
Electronic Supplementary Material (ESI) for Physical Chemistry Chemical Physics.

Nuclear Dynamics in the Metastable Phase of the Solid Acid Caesium Hydrogen Sulfate

Maciej Krzystyniak, Kacper Drużbicki, Felix Fernandez-Alonso

[Full Text](#) | [Contact](#)

Index

1. Sample Preparation and Characterisation

2. Computational Details

3. Structural Parameters of CsHSO₄ phase III

 2.1. PW-DFT vs LCAO-DFT: Cell Volume

 2.2. PW-DFT: Interatomic Distances

4. Phonon Calculations

 3.1. PW-DFT vs LCAO-DFT: INS Spectra

 3.2. PW-DFT vs LCAO-DFT: High-energy v(OH) Stretching Modes

 3.3. PW-DFT: Phase Stability

5. Normal Mode Analysis

 4.1. Factor Group Analysis

 4.2. Normal-mode Animations

References

1. Sample Preparation and Characterisation

CsHSO_4 phase III was synthesized from equimolar aqueous solutions of Cs_2SO_4 and H_2SO_4 using method 1 in Ref. [1]. The resulting crystalline product was dried in a vacuum oven at ambient temperature and kept in a desiccator to avoid water reabsorption. Sample loading was performed in a dry argon glovebox.

The presence (absence) of phase III (II) was ascertained via *in-situ* neutron-diffraction during the MANSE measurements using the methodology previously reported in Ref. [2]. These data are shown in Fig. S1, where the assignment of specific Bragg reflections associated with CsHSO_4 phase III has been performed using the crystallographic data of Itoh *et al.* [3]. From these neutron diffraction data, we also find no evidence for the presence of phase II, which would lead to prominent Bragg reflections at 3.19, 2.98, 2.85, and 2.79 Å, as previously reported by Chisholm and Haile [4].

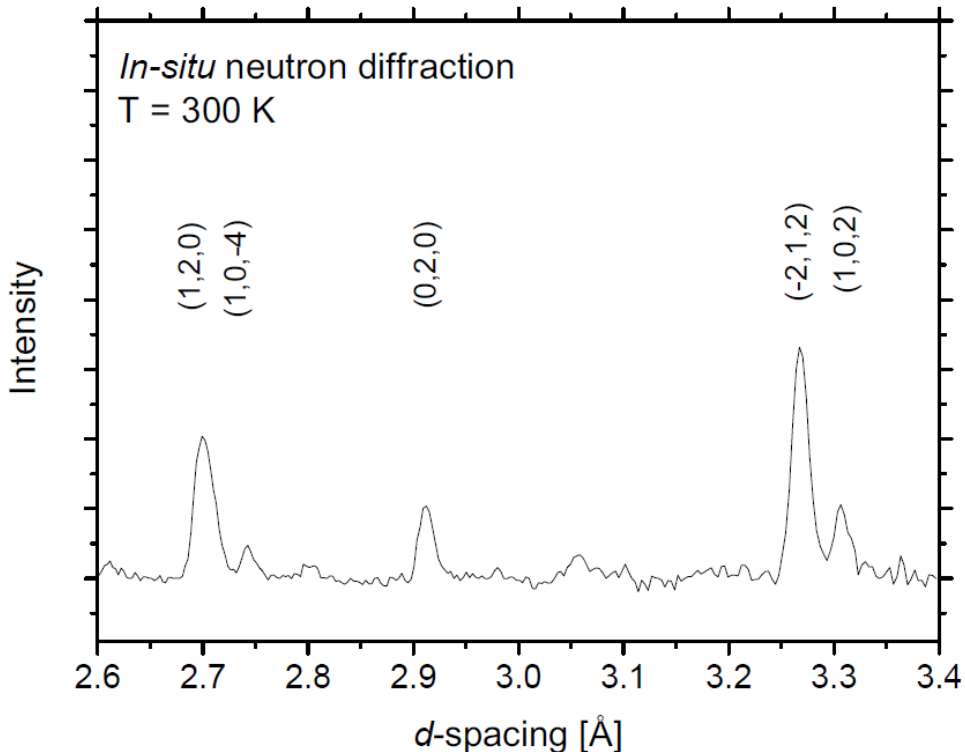


Figure S1 *In-situ* neutron diffraction pattern for CsHSO_4 obtained during the MANSE measurements

In addition to the above experimental checks, the putative presence of residual water in the sample was established from the measured MANSE data, as scattered intensities for a given nuclide are proportional to the product of its relative molar abundance and corresponding neutron-scattering cross section. For pure CsHSO_4 , the expected ratio of proton MANSE intensities relative to heavier species is 3.7531. Experimentally, we find 3.75 ± 0.23 at 300 K, a figure that translates into an upper bound of molar content of H_2O relative to CsHSO_4 of 0.03.

2. Computational Details

In addition to the PW-DFT calculations presented in the main manuscript, solid-state calculations were also performed by employing the linear-combination-of-atomic-orbitals (LCAO) approach as implemented in CRYSTAL14 [5]. To this end, crystal orbitals were expanded as linear combinations of atom-centered Gaussian-type functions. Non-metals were treated with Pople's split-valence double-zeta basis set 6-31G** [6] as well as using a triple-zeta-quality, solid-state-optimized pob-TZVP [7] set of functions. The Hay-Wadt small-core pseudopotential basis-set, constructed by Baranek *et al.* [8], has been applied to Caesium. The computational conditions for the evaluation of the Coulomb and exchange series have adopted truncation tolerances of 10⁻⁸, 10⁻⁸, 10⁻⁸, 10⁻⁸, and 10⁻¹⁶ Ha. The integration of the exchange-correlation contribution to the Fock Matrix was performed with XLGRID. Monkhorst-Pack/Gilat shrinking factors for *k*-point sampling of reciprocal space were set to 16×16. The convergence criterion on total energies for the SCF cycles was set to 10⁻¹² Ha and the total convergence criteria for the geometry optimization process on total energy, atomic displacement and energy gradient were defined as 10⁻¹⁰ Ha, 10⁻⁵ Å, and 5 × 10⁻⁵ Ha/Å⁻¹, respectively. Harmonic frequencies for the fully-optimized crystal structures were calculated with the finite-displacement method.

To date, CRYSTAL14 provides the largest number of exchange-correlation functionals among all solid-state DFT codes available. Various exchange-correlation functionals were adopted, including semi-local GGA (BLYP [9-11], PBE [12,13], PBESol [14,15], SOGGA [16]), meta-GGA (M06-L [17]) as well as standard (B3LYP [10,18,19], PBE0 [20], WC1LYP [10,21], PBESol0 [14,15,20]) and range-separated (HSE06 [22,23]) hybrid (HF/DFT) functionals. In terms of the exchange-enhancement factor $F_x(s)$, the selection of functional varies from 'hard' (BLYP) to 'soft' (PBESol) and includes some recent solid-state-oriented developments like SOGGA, HSE06 or WC1LYP. The influence of vdW interactions is determined here *via* the use of PBE in combination with Grimme's D2 method [24].

From a methodological viewpoint, it is important to emphasize that the use in this work of ad-hoc semiempirical corrections to account for vdW forces is primarily motivated by the observed cancellation of errors between (overly attractive) vdW corrections and (repulsive) contributions from the exchange-correlation functional. As described in more detail below, our detailed comparison with experimental data has not been based on the D2* scheme but, rather, on the more recent method by Tkatchenko-Scheffler (TS) [24]. The latter can account for differences in vdW corrections for a given atom depending on its local environment and, therefore, it is of particular relevance and applicability to the solid state. In TS, s_R is the only adjustable semi-empirical parameter and its value is inversely proportional to the overall contribution of vdW corrections. In our particular case, we have used $s_R = 1.05$ (0.92) for PBE (rPBE), obtaining very similar results in either case. All remaining parameters have not been changed relative to the original TS parametrisation. Furthermore, the original PBE value for s_R is 0.94, yet Bucko *et al.* [25] have recently argued that its average in solids is higher ($s_R = 0.97$) and also closer to our value of 1.05. Since no parametrisation is currently available for rPBE, we can use the 'hard' BLYP and B3LYP schemes as a guide. The original BLYP parametrization gives $s_R = 0.62$ and more recent studies on hydrogen-bonding in water have used a sensibly higher value of $s_R = 0.75$ [26]. The quoted work is based on reference MP2 calculations, which are also known to overestimate vdW interactions. Similarly, a recent parametrisation of B3LYP-TS gives $s_R = 0.84$ [27]. In view of the above, our value of s_R is entirely consistent with those reported in the literature. In addition, we show below that this prescription provides a satisfactory description of available experimental data for CsHSO₄ phase III.

3. Structural Parameters of CsHSO₄ phase III

3.1. PW-DFT vs LCAO-DFT: Cell Volume

The results of the full-structural optimization using PW and LCAO methodologies are presented in Fig. S1. The LCAO calculations confirm the same trend in predicted volumes between ‘hard’ and ‘soft’ GGA. They also show some advantages of solid-state-oriented functionals (*e.g.* HSE06, WC1LYP, PBEsol, SOGGA) and further suggest a promising performance for meta-GGA (M06-L). However, as one can see in the discussion of calculated vibrational spectra further down below, M06-L leads to unreliable phonon structure for this particular system.

When comparing pure- and hybrid-GGA one can note that imposing exact HF-exchange results in relative differences being generally below 5%. While the LCAO scheme allows a much more efficient use of hybrids, non-local functionals are computationally intensive in PW-DFT calculations. None of the tested approaches can properly treat vdW forces. Therefore, the use of dispersion corrections is essential. To date, CRYSTAL14 only allows the use of Grimme’s D2 scheme.

In Fig. S1, one can also note that LCAO calculations result in visibly larger volumes than PW if comparing PBE, PBEsol, or PBE-D2 data (but no more than 5%). PBE-D2* re-parametrization also leads to similar differences, indicating that that LCAO-based parametrizations of *ad hoc* vdW corrections available in the literature (often noted as DFT-D*) may be neither universal nor accurate for PW-DFT calculations and *vice versa*. In summary, we find that none of the tested models using LCAO-DFT could outperform PW-DFT in the calculation of unit-cell volumes for CsHSO₄ phase III.

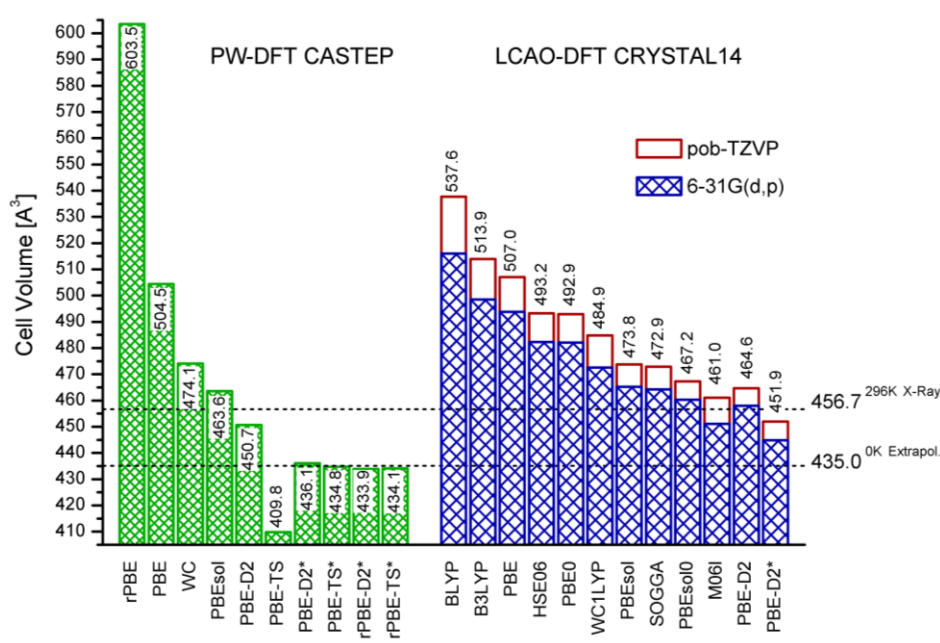


Figure S2 Unit-cell volumes of CsHSO₄ phase III calculated using PW-DFT (CASTEP/DFT/NCPPs/880eV) and LCAO-DFT (CRYSTAL14/DFT/6-31G** and pob-TZVP). Dashed horizontal lines correspond to extrapolated values at 0 K, as discussed in the main text.

3.2. PW-DFT: Interatomic Distances

Figure S2 shows covalent bonds and close-contacts for CsHSO_4 phase III using the data of Ref. [3]. Table S1 compares these data with representative PW-DFT calculations.

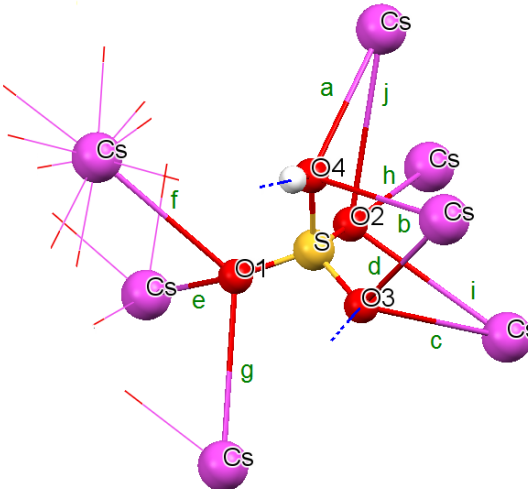


Figure S3 Asymmetric unit and close-contacts in CsHSO_4 phase III after the work of Itoh *et al.* [3]. Labels (a-j) denote $\text{Cs}\cdots\text{O}$ contacts.

Table S1 Selected interatomic distances (\AA) in CsHSO_4 phase III obtained from the PW-DFT calculations. Results of constrained and full-cell relaxation are compared with the experimental data of Ref. [3] shown in the last row of this table. $\text{Cs}\cdots\text{O}$ contacts have been labelled as in Fig. S2.

Method	^{a)} $\text{Cs}\cdots\text{O}(4)$	^{b)} $\text{Cs}\cdots\text{O}(4)$	^{c)} $\text{Cs}\cdots\text{O}(3)$	^{d)} $\text{Cs}\cdots\text{O}(3)$	^{e)} $\text{Cs}\cdots\text{O}(1)$	^{f)} $\text{Cs}\cdots\text{O}(1)$	^{g)} $\text{Cs}\cdots\text{O}(1)$	^{h)} $\text{Cs}\cdots\text{O}(2)$	ⁱ⁾ $\text{Cs}\cdots\text{O}(2)$	^{j)} $\text{Cs}\cdots\text{O}(2)$	S-O(4)	S-O(3)	S-O(1)	S-O(2)	O(4)...O(3)	O(4)...O(1)	O(4)...O(2)	O(3)...O(1)	O(3)...O(2)	O(1)...O(2)	O(4)-H	H...O(3)	O(3)...O(4)
PBE Fixed-Opt	3.107	3.468	3.159	3.376	3.133	3.235	3.292	3.105	3.334	3.524	1.576	1.476	1.444	1.434	2.431	2.376	2.412	2.407	2.442	1.032	1.527	2.558	
rPBE Fixed-Opt	3.093	3.479	3.130	3.387	3.159	3.219	3.266	3.124	3.397	3.557	1.589	1.478	1.449	1.438	2.441	2.442	2.385	2.385	2.418	2.449	1.021	1.568	2.589
WC Fixed-Opt	3.125	3.456	3.181	3.360	3.114	3.261	3.336	3.110	3.270	3.455	1.554	1.475	1.438	1.430	2.415	2.416	2.364	2.402	2.392	2.431	1.055	1.447	2.502
PBEsol Fixed-Opt	3.128	3.448	3.183	3.364	3.116	3.264	3.329	3.111	3.280	3.447	1.552	1.477	1.439	1.431	2.416	2.417	2.365	2.404	2.393	2.434	1.061	1.435	2.496
PBE Full-Opt	3.208	3.574	3.292	3.413	3.238	3.408	3.583	3.213	3.322	3.604	1.584	1.475	1.444	1.438	2.438	2.441	2.376	2.419	2.408	2.444	1.025	1.572	2.596
rPBE Full-Opt	3.399	3.909	3.363	4.104	3.550	3.551	3.614	3.327	3.338	3.561	1.606	1.467	1.454	1.452	2.455	2.466	2.385	2.437	2.433	2.439	1.005	1.702	2.703
PBEsol Full-Opt	3.144	3.447	3.203	3.358	3.129	3.302	3.383	3.120	3.277	3.452	1.553	1.477	1.439	1.432	2.416	2.418	2.365	2.405	2.393	2.435	1.060	1.440	2.500
WC Full-Opt	3.159	3.469	3.219	3.351	3.151	3.341	3.492	3.134	3.258	3.484	1.556	1.475	1.437	1.431	2.416	2.419	2.363	2.405	2.391	2.433	1.052	1.459	2.511
PBE-D2 Full-Opt	3.158	3.357	3.222	3.313	3.111	3.197	3.219	3.172	3.319	3.420	1.578	1.476	1.444	1.434	2.435	2.428	2.377	2.408	2.411	2.444	1.029	1.539	2.568
PBE-TS Full-Opt	3.007	3.459	3.051	3.391	2.961	3.083	3.112	2.938	3.438	3.475	1.556	1.474	1.445	1.431	2.420	2.409	2.378	2.394	2.407	2.436	1.045	1.458	2.504
PBE-D2* Full-Opt	3.129	3.318	3.183	3.280	3.060	3.137	3.156	3.164	3.326	3.410	1.575	1.476	1.444	1.433	2.434	2.422	2.379	2.403	2.412	2.443	1.031	1.527	2.558
PBE-TS* Full-Opt	2.994	3.372	3.006	3.275	3.157	3.351	3.360	2.946	3.772	3.794	1.559	1.481	1.447	1.429	2.410	2.424	2.374	2.412	2.398	2.446	1.053	1.427	2.479
rPBE-D2* Full-Opt	3.140	3.353	3.149	3.302	3.093	3.130	3.158	3.232	3.478	3.608	1.590	1.477	1.451	1.438	2.450	2.430	2.399	2.404	2.429	2.450	1.019	1.581	2.600
rPBE-TS* Full-Opt	3.156	3.667	3.216	3.573	3.022	3.118	3.149	3.057	3.406	3.458	1.578	1.470	1.452	1.440	2.444	2.426	2.392	2.406	2.426	2.436	1.021	1.577	2.598
X-Ray 296K	3.114	3.503	3.172	3.403	3.122	3.235	3.287	3.105	3.350	3.513	1.570	1.469	1.439	1.428	2.417	2.413	2.367	2.399	2.402	2.439	1.256	1.435	2.555

4. Phonon Calculations

4.1. PW-DFT vs LCAO-DFT: INS Spectra

Calculated INS spectra using PW- and LCAO-DFT are presented in Fig. S3, while a detailed mode assignment is given in Section 4 below. For CsHSO₄ phase III, we find that PW-DFT calculations provide an overall closer match to available experimental data than CRYSTAL14/DFT/6-31G**, thereby justifying their eventual use in the detailed interpretation of the INS and MANSE results in the main manuscript.

Analyzing the Γ -point LCAO calculations, INS spectra display a prominent band around 100 meV, corresponding to *out-of-plane* OH bending motions. There is also an upward shift of vibrational energies accompanying the transition from ‘hard’ (BLYP) to ‘soft’ (PBEsol) functionals. If compared to pure-GGA analogs, no advantage in the use of hybrid functionals could be found in the present case. Also, meta-GGA (M06-L) calculations result in an unreliable phonon structure, poorly matching the experimental INS data. Such an effect may be partially attributed to the high degree of parametrization of M06-L to account for long-range dispersive interactions in molecular systems. On the whole, BLYP, PBE, and PBEsol provide acceptable results, with a similar intensity distribution over 10 meV, that is, in the internal-mode range.

The PW-DFT simulations were performed both at the Γ -point and by averaging the spectra calculated over 37 q -points. While the INS spectrum is not greatly affected by mode dispersion in the intermolecular range, such effects are of significance for the lattice-modes below 10 meV. A detailed inspection of phonon energies and associated intensities clearly shows that rPBE-TS* and PBE-TS* provide an improved agreement with experimental data relative to other local-GGA models. Tkatchenko-Scheffler (TS) corrections [24] were also found to give better agreement with experimental results than Grimme’s (D2) scheme.

Unlike any other DFT model for CsHSO₄ phase III explored in this work, rPBE-TS* and PBE-TS* also provide a reasonable agreement at the lowest energy transfers. In this region, the most intense doublet around 15 meV has been generally attributed to Cs···O stretching modes. These close-contacts clearly depend on cell volume. Therefore, the position of related stretching modes largely dictates the accuracy of our computational description of the Cs···O framework.

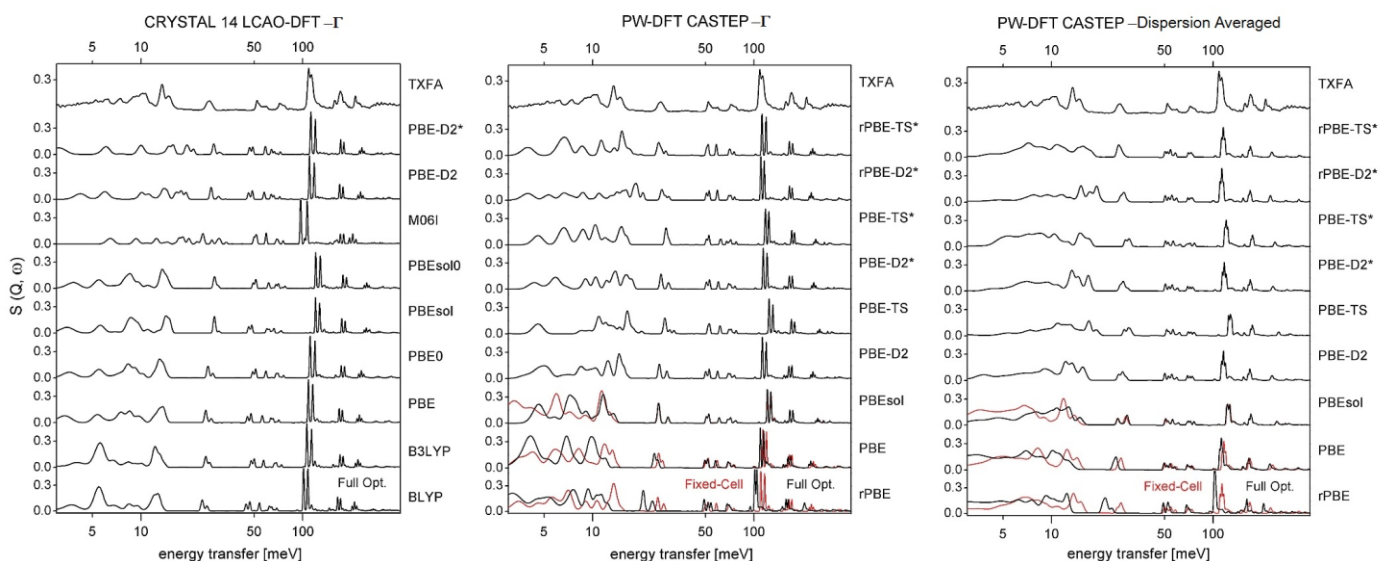


Figure S4 Experimental INS spectrum of CsHSO₄ phase III [28] compared with DFT predictions using several exchange-correlation functionals (PW-DFT/CASTEP/NCPPs/880eV and LCAO-DF/CRYSTAL14/6-31G**). The theoretical results refer to Γ -point simulations (LCAO-DFT and PW-DFT) as well as dispersion-averaging over the 37 q -points (PW-DFT). All computed spectra include overtones and combination bands up to tenth order.

As mentioned above, explicit inclusion of vdW corrections has certain advantages over the use of a fixed-cell scheme based on experimental values, as the latter approach gives rise to spurious internal stresses in the crystal structure and concomitant shifts in calculated vibrational frequencies. Such an effect is clearly visible in Fig. S3 for

rPBE. Comparing the fixed-cell and full-optimization schemes, one can note that internal stresses have a profound effect in the resulting INS spectrum over the entire energy-transfer range.

It is also worth noting that commonly used, fixed-cell PW-PBE calculations give reasonable agreement with experimental data. We also observe that the same fixed-cell methodology applied to LCAO calculations tends to give some large and spurious upward shifts. Surprisingly, such an effect is quite prominent with pob-TZVP.

In Fig. S4, we present the influence of basis-set choice on the INS spectrum as calculated using a fixed cell and either PW- or LCAO-DFT schemes. One can clearly see that a PW energy cutoff of 880 eV results in a well-converged internal-mode spectrum, while providing a good compromise between numerical quality and computational cost. Alternatively to linear-response schemes, the Γ -point spectrum has also been calculated using finite displacements with highly-accurate, *on-the-fly* ultrasoft-pseudopotentials (USPPs). Since in this case the total-energy converges with a much-lower number of PWs, the resulting data tends to approach the one calculated with norm-conserving pseudopotentials (NCPPs) and a PW cutoff of 1500eV. In summary, the influence of basis-set size on calculated PW-DFT spectra is rather small.

Somewhat surprisingly, we observe significant differences between the 6-31G** and pob-TZVP predictions, as shown in Fig. S4. Such an effect might be attributed to basis-set superposition errors (BSSEs). Small basis sets might stabilize the crystal structure more due to a larger BSSE, compensating the deficiency of semi-local PBE to treat vdW interactions and, therefore, giving a smaller (and spurious) internal stress and smaller concomitant shifts in calculated INS spectra. However, the PW-DFT calculations do not support such an assumption, since they are free of BSSEs and do not lead to a significant upward energy shifts with increasing energy cutoff. The nature of this effect for pob-TZVP may be, hence, more intricate than anticipated.

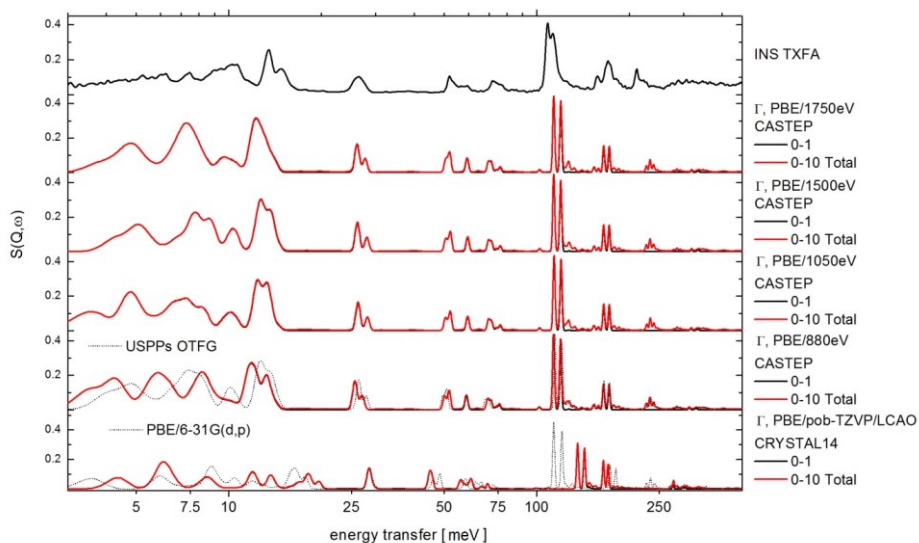


Figure S5 INS spectra of CsHSO₄ phase III for different basis sets. For further details, see the text.

4.2. PW-DFT vs LCAO-DFT: High-energy v(OH) Stretching Modes

High-energy v(OH) stretching modes are hardly discernible from the INS data, due to recoil effects arising from the high momentum-transfers in this energy region. According to the room-temperature FT-Raman study by Baran and Marchewka [29], these modes appear at ~300 and 350 meV. According to Fig. S5, their precise location is strongly dependent on the choice of functional, with differences of up to nearly 100 meV between ‘hard’ and ‘soft’ implementations of GGA. As mentioned above, inclusion of exact HF-exchange results in an upward shift of v(OH) energies, further increasing with HF fraction and softening of the GGA functional. The inclusion of vdW corrections was also found to be of relevance for these high-energy modes.

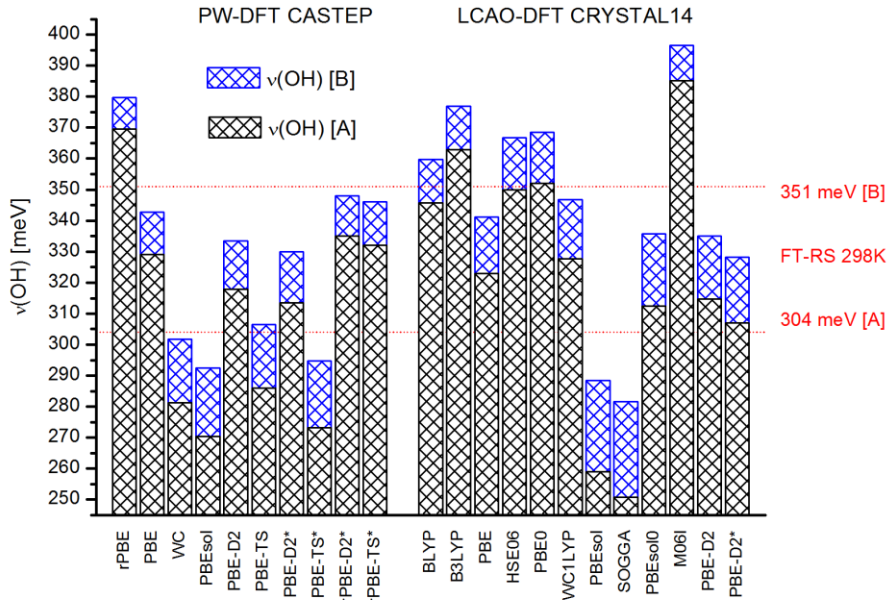


Figure S6 Average energy of the highest-frequency OH stretching modes (A and B symmetry) in CsHSO₄ phase III calculated using PW-DFT (CASTEP/DFT/NCPGs/880eV) and LCAO-DFT (CRYSTAL14/DFT/6-31G**) for fully optimized crystal structures. Dotted horizontal lines correspond to FT-Raman energies reported by Baran and Marchewka [29].

4.3. PW-DFT: Phase Stability

In most cases, the use of the pure GGA functional results in the occurrence of multiple mechanical instabilities beyond the Γ -point. Each soft mode has been characterized in terms of its energy and related q -point, as shown in Table S2. The inclusion of vdW corrections results in fully stable equilibrium structures with $P2_1/c$ symmetry. The occurrence of soft-modes in the fixed-cell PBE and rPBE calculations is illustrated in Fig. S6.

Table S2 Analysis of mechanical stability of CsHSO₄ phase III using PW-DFT. The lattice-dynamics calculations were performed with several exchange-correlation functionals (CASTEP/NCPGs/880eV). Each soft mode is defined by its frequency (in meV) and related q -point coordinate.

CASTEP PW-DFT	energy transfer [meV]	q -point
rPBE Fixed	-1.1	[-0.50 0.00 0.25]
rPBE Full		No Soft Modes
PBE Fixed	-0.7	[0.00 0.00 0.25]
PBE Full	-2.1	[0.00 0.25 0.00]
	-2.6	[-0.50 0.25 0.00]
	-1.4	[-0.50 0.00 0.00]
	-1.5	[-0.50 0.00 0.25]
	-0.3	[-0.50 0.00 0.50]
	-1.0	[-0.50 0.25 0.50]
PBESol Fixed	-0.9	[0.00 0.25 0.00]
	-2.4	[-0.50 0.25 0.00]
	-2.0	[-0.50 0.00 0.00]
	-0.9	[-0.50 0.00 0.25]
PBESol Full		
PBE-D2 Full		
PBE-TS Full		
PBE-D2* Full		No Soft Modes
PBE-TS* Full		
rPBE-D2* Full		
rPBE-TS* Full		

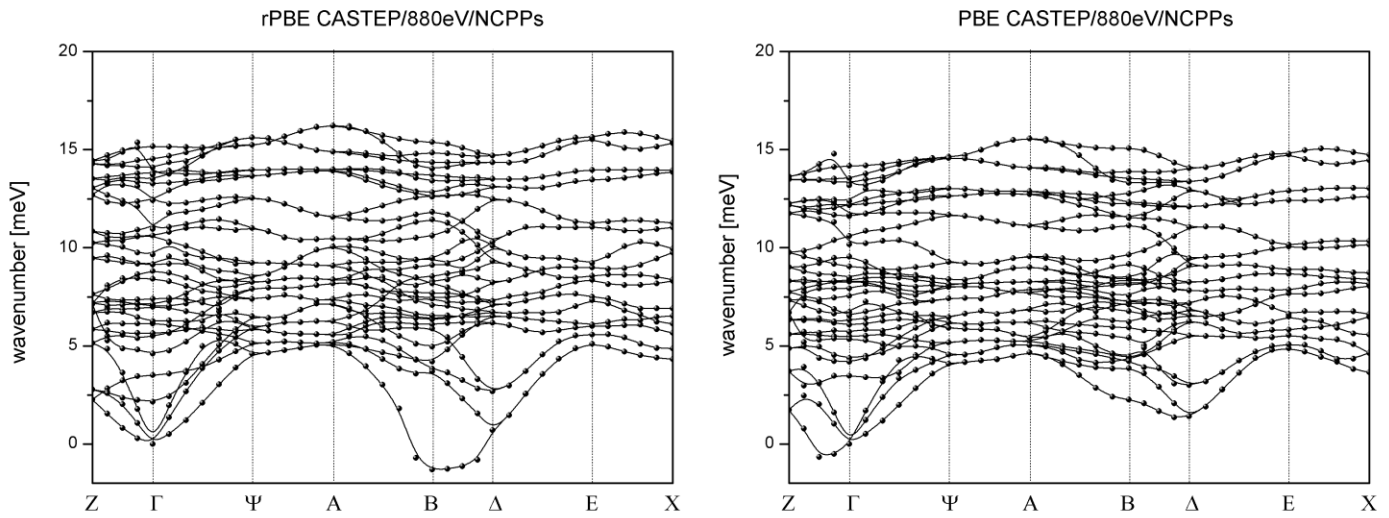


Figure S7 Low-energy phonon-dispersion relations for CsHSO_4 phase III calculated with rPBE and PBE functionals and a fixed cell using available experimental data at 296 K [3].

[Previous: Structural Parameters of CsHSO_4 phase III] [Next: Normal Mode Analysis] [Index]

5. Normal Mode Analysis

5.1. Factor Group Analysis

The crystallographic structure of CsHSO₄ phase III (*P*2₁/*c*) can be considered as consisting of two pseudo cells. Each pseudo cell can be treated as a sub-lattice of *P*2₁ symmetry. In the *P*2₁/*c* structure, the [A] and [B] symmetry modes further split into *gerade* and *ungerade* species. Therefore, fourfold degeneracy is expected for each type of vibration.

The space group of the unit-cell is *P*2₁/*c* (No. 14), its point group is C_{2h} (2/m) and Z = 4.

Mechanical representation

$$M = 21A_g + 21A_u + 21B_g + 21B_u$$

Acoustic and Optic modes:

$$\Gamma_{\text{acoustic}} = A_u + 2B_u$$

$$\Gamma_{\text{optic}} = 21A_g + 20A_u + 21B_g + 19B_u$$

The space group of the sub-lattice is *P*2₁ (No. 4), its point group is C₂ (2) and Z = 2.

Mechanical representation

$$M = 21A + 21B$$

Acoustic and Optic modes:

$$\Gamma_{\text{acoustic}} = A + 2B$$

$$\Gamma_{\text{optic}} = 20A + 19B$$

5.2. Normal-mode Animations

The results of rPBE-TS* PW-DFT calculations are analyzed in detail below. For ease of visualization, all vibrational-mode animations are presented using the supercell as well as the C₂-symmetry pseudo cell, as illustrated in Fig. S7. Web links to interactive animations as well as approximate mode assignments can be found in Table S3.

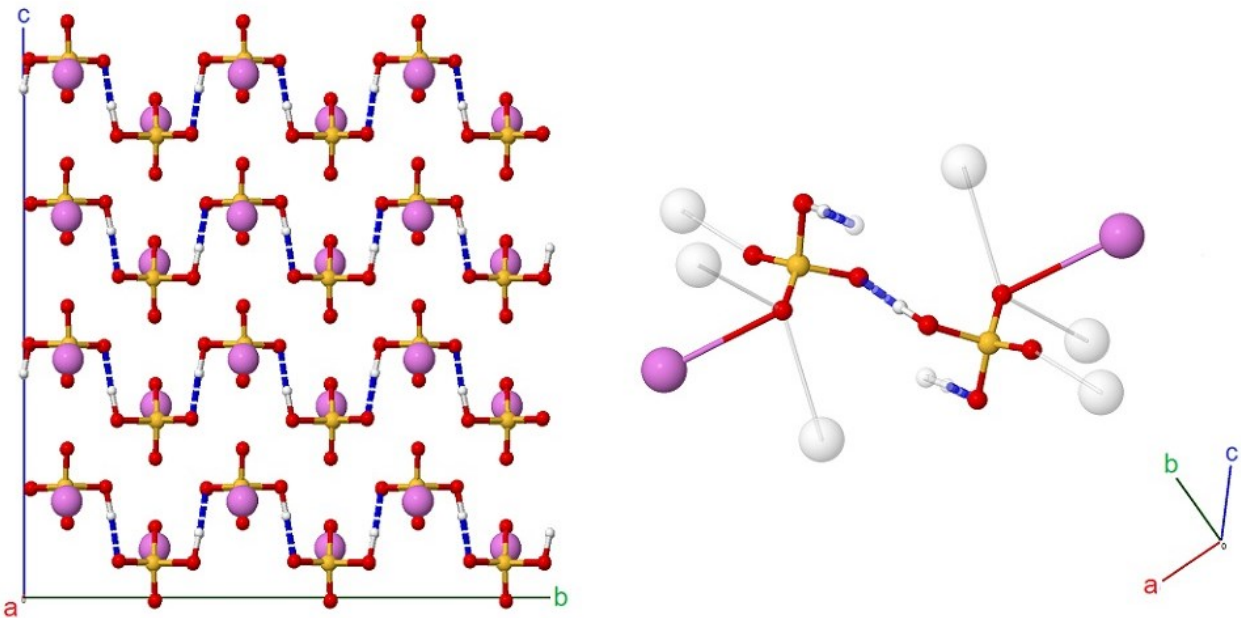


Figure S8 {3 3 2} supercell projection of CsHSO₄ phase III (left) along with a close-view on the hydrogen-bonded sub-lattice (right). The close contacts are shown in translucent white. The equilibrium structure shown has been obtained from fully optimised rPBE-TS* calculations.

Table S3 Γ -point vibrational energies in CsHSO₄ phase III from fully optimized rPBE-TS* calculations (see the manuscript for details). Mode animations are given for supercell (Crystal) and molecular (Sub-Lattice) projections. The rightmost column provides an approximate description of each mode.

No.	v [meV]	S (Q,ω) [%]	Symmetry	Animation		Description
1	0.00	-	[Au]	Crystal	Sub-Lattice	acoustic → b
2	0.00	-	[Bu]	Crystal	Sub-Lattice	acoustic → c
3	0.00	-	[Bu]	Crystal	Sub-Lattice	acoustic → a
4	1.48	6.8	[Bg]	Crystal	Sub-Lattice	transl. HSO ₄ → a / transl. Cs…Cs → c
5	4.09	6.7	[Bg]	Crystal	Sub-Lattice	lib. HSO ₄ ∠ ac / transl. Cs…Cs → c
6	5.99	3.1	[Bu]	Crystal	Sub-Lattice	lib. HSO ₄ ∠ ab / transl. Cs…Cs → c
7	6.53	10.4	[Ag]	Crystal	Sub-Lattice	lib. HSO ₄ ∠ ab / transl. Cs…Cs → b
8	6.96	8.4	[Au]	Crystal	Sub-Lattice	lib. HSO ₄ ∠ ab / transl. Cs…Cs → c
9	7.22	2.7	[Bg]	Crystal	Sub-Lattice	lib. HSO ₄ ∠ ac / transl. Cs…Cs → a
10	8.45	1.5	[Ag]	Crystal	Sub-Lattice	lib. HSO ₄ ∠ ab / transl. Cs…Cs → c
11	8.46	4.0	[Au]	Crystal	Sub-Lattice	lib. HSO ₄ ∠ ab / transl. Cs…Cs → c
12	9.03	4.1	[Ag]	Crystal	Sub-Lattice	lib. HSO ₄ ∠ ab / transl. Cs…Cs → c
13	11.16	1.4	[Ag]	Crystal	Sub-Lattice	transl. HSO ₄ → c
14	11.39	8.8	[Au]	Crystal	Sub-Lattice	lib. HSO ₄ ∠ ab
15	11.49	3.9	[Bg]	Crystal	Sub-Lattice	transl. HSO ₄ → c / transl. Cs…Cs → c
16	12.33	3.4	[Bu]	Crystal	Sub-Lattice	transl. HSO ₄ → c / transl. Cs…Cs → c
17	13.22	1.1	[Bu]	Crystal	Sub-Lattice	δ(Cs-O-S)
18	13.53	0.5	[Bg]	Crystal	Sub-Lattice	γ(Cs-O-S)
19	13.73	3.2	[Ag]	Crystal	Sub-Lattice	γ(Cs-O-S)
20	13.82	0.5	[Au]	Crystal	Sub-Lattice	δ(Cs-O-S)
21	13.97	0.7	[Ag]	Crystal	Sub-Lattice	δ(Cs-O-S)
22	15.03	0.6	[Au]	Crystal	Sub-Lattice	δ(Cs-O-S)
23	15.09	5.4	[Bg]	Crystal	Sub-Lattice	ν(Cs…O)
24	15.16	14.6	[Ag]	Crystal	Sub-Lattice	γ(Cs-O-S)
25	15.33	1.6	[Bu]	Crystal	Sub-Lattice	γ(Cs-O-S)
26	15.84	8.4	[Au]	Crystal	Sub-Lattice	ν(Cs…O)
27	16.56	5.5	[Bu]	Crystal	Sub-Lattice	ν(Cs…O)
28	17.19	3.9	[Au]	Crystal	Sub-Lattice	ν(Cs…O)

29	17.25	4.3	[Bg]	Crystal	Sub-Lattice		v(Cs··O)
30	17.32	2.2	[Bu]	Crystal	Sub-Lattice		v(Cs··O)
31	18.43	1.6	[Ag]	Crystal	Sub-Lattice		v(Cs··O)
32	19.89	1.3	[Bg]	Crystal	Sub-Lattice		v(Cs··O)
33	25.35	10.0	[Au]	Crystal	Sub-Lattice		v(O··O) / δ(Cs-O-S)
34	25.99	9.8	[Ag]	Crystal	Sub-Lattice		v(O··O) / δ(Cs-O-S)
35	26.79	6.6	[Bu]	Crystal	Sub-Lattice		γ(Cs-O-S) / v(O··O)
36	28.45	5.6	[Bg]	Crystal	Sub-Lattice		γ(Cs-O-S) / v(O··O)
37	50.69	3.0	[Bg]	Crystal	Sub-Lattice		δ _(CsO-S-O_{CS}) + δ _(H_{O-S-O-H})
38	50.72	7.0	[Ag]	Crystal	Sub-Lattice		δ _(CsO-S-O_{CS}) + δ _(H_{O-S-O-H})
39	50.76	7.5	[Bu]	Crystal	Sub-Lattice		δ _(CsO-S-O_{CS}) + δ _(H_{O-S-O-H})
40	51.18	1.4	[Au]	Crystal	Sub-Lattice		δ _(CsO-S-O_{CS}) + δ _(H_{O-S-O-H})
41	51.95	8.7	[Au]	Crystal	Sub-Lattice		δ _(CsO-S-O-H) + δ _(CsO-S-O_H)
42	52.23	8.7	[Ag]	Crystal	Sub-Lattice		δ _(CsO-S-O-H) + δ _(CsO-S-O_H)
43	58.19	9.8	[Bu]	Crystal	Sub-Lattice		δ _(CsO-S-O-H) + δ _(CsO-S-O_H)
44	58.67	9.8	[Bg]	Crystal	Sub-Lattice		δ _(CsO-S-O-H) + δ _(CsO-S-O_H)
45	69.96	3.6	[Bu]	Crystal	Sub-Lattice		δ _(CsO-S-O_{CS}) - δ _(H_{O-S-O-H})
46	70.28	3.8	[Au]	Crystal	Sub-Lattice		δ _(CsO-S-O_{CS}) - δ _(H_{O-S-O-H})
47	70.41	4.5	[Ag]	Crystal	Sub-Lattice		δ _(CsO-S-O_{CS}) - δ _(H_{O-S-O-H})
48	70.45	3.6	[Bg]	Crystal	Sub-Lattice		δ _(CsO-S-O_{CS}) - δ _(H_{O-S-O-H})
49	71.33	0.5	[Bu]	Crystal	Sub-Lattice		δ _(CsO-S-O-H) - δ _(CsO-S-O_H)
50	71.34	2.8	[Au]	Crystal	Sub-Lattice		δ _(CsO-S-O_{CS}) - δ _(H_{O-S-O-H})
51	71.51	6.1	[Bg]	Crystal	Sub-Lattice		δ _(CsO-S-O-H) - δ _(CsO-S-O_H)
52	71.62	6.5	[Ag]	Crystal	Sub-Lattice		δ _(CsO-S-O_{CS}) - δ _(H_{O-S-O-H})
53	72.93	0.8	[Bu]	Crystal	Sub-Lattice		γ _(CsO-S-O_{CS})
54	73.13	1.7	[Bg]	Crystal	Sub-Lattice		γ _(CsO-S-O_{CS})
55	75.02	3.6	[Ag]	Crystal	Sub-Lattice		γ _(H_{O-S-O-H})
56	75.55	3.6	[Au]	Crystal	Sub-Lattice		γ _(H_{O-S-O-H})
57	101.81	0.6	[Au]	Crystal	Sub-Lattice		v(SO _H)
58	102.10	1.1	[Bu]	Crystal	Sub-Lattice		v(SO _H)
59	102.71	1.0	[Ag]	Crystal	Sub-Lattice		v(SO _H)
60	102.99	1.0	[Bg]	Crystal	Sub-Lattice		v(SO _H)
61	112.11	100.0	[Ag]	Crystal	Sub-Lattice		γ(OH)
62	112.12	100.0	[Au]	Crystal	Sub-Lattice		γ(OH)
63	118.72	71.2	[Bg]	Crystal	Sub-Lattice		γ(OH)
64	118.83	71.2	[Bu]	Crystal	Sub-Lattice		γ(OH)
65	122.62	0.6	[Au]	Crystal	Sub-Lattice		v _{ss(CsOSO_{CS})} + v(SO··H)
66	122.91	0.6	[Ag]	Crystal	Sub-Lattice		v _{ss(CsOSO_{CS})} + v(SO··H)
67	127.82	0.4	[Bu]	Crystal	Sub-Lattice		v _{ss(CsOSO_{CS})} + v(SO··H)
68	128.29	0.5	[Bg]	Crystal	Sub-Lattice		v _{ss(CsOSO_{CS})} + v(SO··H)
69	141.40	0.7	[Bu]	Crystal	Sub-Lattice		v _{ss(CsOSO_{CS})} - v(SO··H)
70	142.70	0.7	[Bg]	Crystal	Sub-Lattice		v _{ss(CsOSO_{CS})} - v(SO··H)
71	143.61	0.4	[Ag]	Crystal	Sub-Lattice		v _{ss(CsOSO_{CS})} - v(SO··H)
72	143.67	0.6	[Au]	Crystal	Sub-Lattice		v _{ss(CsOSO_{CS})} - v(SO··H)
73	149.74	3.0	[Bu]	Crystal	Sub-Lattice		v _{ass(CsOSO_{CS})} / δ(OH)
74	152.76	4.0	[Bg]	Crystal	Sub-Lattice		v _{ass(CsOSO_{CS})} / δ(OH)
75	153.23	2.3	[Ag]	Crystal	Sub-Lattice		v _{ass(CsOSO_{CS})} / δ(OH)
76	155.92	3.3	[Au]	Crystal	Sub-Lattice		v _{ass(CsOSO_{CS})} / δ(OH)
77	165.44	25.3	[Ag]	Crystal	Sub-Lattice		δ(OH)
78	165.67	26.8	[Au]	Crystal	Sub-Lattice		δ(OH)
79	173.34	19.1	[Bu]	Crystal	Sub-Lattice		δ(OH)
80	173.78	18.2	[Bg]	Crystal	Sub-Lattice		δ(OH)
81	331.99	2.9	[Au]	Crystal	Sub-Lattice		v(OH)
82	332.30	2.9	[Ag]	Crystal	Sub-Lattice		v(OH)
83	344.69	2.4	[Bu]	Crystal	Sub-Lattice		v(OH)
84	347.43	2.3	[Bg]	Crystal	Sub-Lattice		v(OH)

[\[Previous: Phonon Calculations\]](#) [\[Next: References\]](#) [\[Index\]](#)

References

1. Ph. Colombari, M. Pham-Thi, and A. Novak, *Solid State Ionics*, 1987, **24**, 193.
2. M. Krzstyniak, M. A. Adams, A. Lovell, N. T. Skipper, S. M. Bennington, J. Mayers and F. Fernandez-Alonso, *Faraday Discuss.*, 2011, **151**, 171.
3. K. Itoh, T. Ukedo, T. Ozaki and E. Nakamura, *Acta Cryst. C*, 1990, **46**, 358.
4. C. R. I. Chisholm and S. M. Haile, *Mater. Res. Bull.*, 2000, **35**, 999.
5. R. Dovesi, R. Orlando, A. Erba, C. M. Zicovich-Wilson, B. Civalleri, S. Casassa, L. Maschio, M. Ferrabone, M. De La Pierre, P. DArco, Y. Noel, M. Causa, M. Rerat and B. Kirtman, *Int. J. Quantum Chem.*, 2014, **114**, 1287.
6. R. Krishnan, J. S. Binkley, R. Seeger and J. A. Pople, *J. Chem. Phys.*, 1980, **72**, 650.
7. M. F. Peintinger, D. Vilela Oliveira and T. Bredow, *J. Comp. Chem.*, 2013, **36**, 451.
8. [www.crystal.unito.it/Basis_Sets/caesium.html#Cs_SC_HAYWSC-31\(1d\)G_baranek_2013_CsTaO3](http://www.crystal.unito.it/Basis_Sets/caesium.html#Cs_SC_HAYWSC-31(1d)G_baranek_2013_CsTaO3)
9. A. D. Becke, *Phys. Rev. A*, 1988, **38**, 3098.
10. C. Lee, W. Yang and R. G. Par, *Phys. Rev. B*, 1988, **37**, 785.
11. B. Miehlich, A. Savin, H. Stoll and H. Press, *Chem. Phys. Lett.*, 1989, **157**, 200.
12. J. P. Perdew and K. Burke, *Phys. Rev. Lett.*, 1996, **77**, 3865.
13. J. P. Perdew and K. Burke, *Phys. Rev. Lett.*, 1997, **78**, 1396.
14. J. P. Perdew, A. Ruzsinszky, G. I. Csonka, O. A. Vydrov, G. E. Scuseria, L. A. Constantin, X. Zhou and K. Burke, *Phys. Rev. Lett.*, 2008, **100**, 136406.
15. J. P. Perdew, A. Ruzsinszky, G. I. Csonka, O. A. Vydrov, G. E. Scuseria, L. A. Constantin, X. Zhou and K. Burke, *Phys. Rev. Lett.*, 2009, **102**, 039902.
16. Y. Zhao and D. G. Truhlar, *J. Chem. Phys.*, 2008, **128**, 184109.
17. Y. Zhao and D. G. Truhlar, *J. Chem. Phys.*, 2006, **125**, 194101.
18. A. D. Becke, *J. Chem. Phys.*, 1993, **98**, 5648.
19. P. J. Stephens, F. J. Devlin, C. F. Chabalowski and M. J. Frisch, *J. Phys. Chem.*, 1994, **98**, 11623.
20. C. Adamo and V. Barone, *J. Chem. Phys.*, 1999, **110**, 6158.
21. Z. Wu and R. E. Cohen, *Phys. Rev. B*, 2006, **73**, 235116.
22. J. Heyd, G. E. Scuseria and M. Ernzerhof, *J. Chem. Phys.*, 2003, **118**, 8207.
23. J. Heyd, G. E. Scuseria and M. Ernzerhof, *J. Chem. Phys.*, 2006, **124**, 219901.
24. S. Grimme, *J. Comput. Chem.*, 2006, **27**, 1787.
24. A. Tkatchenko and M. Scheffler, *Phys. Rev. Lett.*, 2009, **102**, 073005.
25. T. Bučko, S. Lebègue, J. Hafner and J. G. Ángyán, *Phys. Rev. B*, 2014, **87**, 064110.
26. B. Santra, Ph.D. Thesis ‘Density-Functional Theory Exchange-Correlation Functionals for Hydrogen Bonds in Water’, Technischen Universität Berlin, 2010, www.chem.ucl.ac.uk/ice/docs/santra_biswajit.pdf
27. N. Marom, A. Tkatchenko, M. Rossi, V. V. Gobre, O. Hod, M. Scheffler and L. Kronik, *J. Chem. Theory Comput.*, 2011, **7**, 3944.
28. A. V. Belushkin, M. A. Adams, A. I. Kolesnikov and L. A. Shuvalov, *J. Phys.: Condens. Matter*, 1994, **6**, 5823.
27. J. Baran and M. K. Marchewka, *J. Mol. Struct.*, 2002, **614**, 133.